


 Cite this: *RSC Adv.*, 2022, **12**, 8862

## Biodegradable $\text{MoO}_x@\text{MB}$ incorporated hydrogel as light-activated dressing for rapid and safe bacteria eradication and wound healing†

 Yifan Wang,<sup>a</sup> Huiqin Yao,<sup>\*a</sup> Yan Zu<sup>\*b</sup> and Wenyan Yin<sup>b</sup>

Wounds infected with drug-resistant bacteria are hard to treat, which remains a serious problem in clinical practice. An innovative strategy for treating wound infections is thus imperative. Herein, we describe the construction of a nanocomposite from biocompatible poly(vinyl alcohol) (PVA)/polyethylene glycol (PEG) hydrogel loaded biodegradable  $\text{MoO}_x$  nanoparticles (NPs) and photosensitizer methylene blue (MB), denoted as  $\text{MoO}_x@\text{MB-hy}$ . By incorporating  $\text{MoO}_x@\text{MB}$  NPs, the nanocomposite hydrogel can act as a photoactivated wound dressing for near-infrared-II 1064 nm and 660 nm laser synergistic photothermal-photodynamic therapy (PTT-PDT). The key to PTT-induced heat becomes the most controllable release of MB from  $\text{MoO}_x@\text{MB-hy}$  to produce more  ${}^1\text{O}_2$  under 660 nm irradiation. Importantly,  $\text{MoO}_x@\text{MB-hy}$  can consume glutathione (GSH) and trap bacteria nearer to the distance limit of ROS damage to achieve a self-migration-enhanced accumulation of reactive oxygen species (ROS), thereby conquering the intrinsic shortcomings of short diffusion distance and lifetime of ROS. Consequently,  $\text{MoO}_x@\text{MB-hy}$  has high antibacterial efficiencies of 99.28% and 99.16% against Amp<sup>r</sup> *E. coli* and *B. subtilis* within 15 min. Moreover, the light-activated strategy can rapidly promote healing in wounds infected by drug-resistant bacteria. This work paves a way to design a novel nanocomposite hydrogel dressing for safe and highly-efficient antibacterial therapy.

Received 14th February 2022  
 Accepted 7th March 2022

DOI: 10.1039/d2ra00963c  
[rsc.li/rsc-advances](http://rsc.li/rsc-advances)

### 1. Introduction

Bacteria-induced wound infections have become a severe threat to human health. Although antibiotics have been used to combat bacterial infections, the abuse/overuse of antibiotics has brought about the serious generation of drug-resistant bacteria.<sup>1-3</sup> Consequently, it is imperative to develop safe, highly effective and non-antibiotic therapeutic strategies. Nanomaterials have been investigated as therapeutic agents, relying on surface modification with biocompatible moieties.<sup>4-7</sup> To date, phototherapeutic strategies based on nanomaterials, including photothermal therapy (PTT) and photodynamic therapy (PDT), constitute a powerful armory to resist drug-resistant bacteria due to their unique advantages, such as minimal invasiveness, high spatial and temporal controllable precision of light and avoidance of drug-resistant bacteria.<sup>8-10</sup> The duration of dual-light therapy is short and the

phototherapy instrument is easily carried. There are similar phototherapy instruments in clinical practice, such as red light phototherapy instruments to treat skin wounds, which can easily relieve the pain of patients.<sup>11</sup> These phototherapeutic nanomaterials mainly include carbon-based nanomaterials, transition metal sulfides/oxides, noble metals, *etc.* In particular, the combination of PDT and PTT in one system is a promising strategy to improve therapeutic efficiency and minimize side effects for localized wound treatment.<sup>12-14</sup>

Strikingly, as important transition metal oxides, defect-structured molybdenum oxide ( $\text{MoO}_x$ ,  $1 < x \leq 3$ ) nanomaterials have become a research focus in phototherapy, and antibacterial and antitumor biomedical applications owing to their advantages, such as a strong near-infrared (NIR) photothermal conversion effect, enzyme-like catalytic activity (ROS scavenging/production) and good biocompatibility.<sup>15-17</sup> For example,  $\text{MoO}_{3-x}$  nanodots with ROS scavenging ability could bind firmly with bacteria in some forms for bacterial sterilization.<sup>15</sup> Molybdenum is also an important microelement in the living body.<sup>18</sup>  $\text{MoO}_x$  nanomaterials degrade naturally in the physiological environment forming harmless  $\text{MoO}_4^{2-}$ .<sup>19,20</sup> In particular, defect-structured  $\text{MoO}_x$  nanomaterials with localized surface plasmon resonance (LSPR) possess very high NIR-II photothermal absorption efficiency, which is beneficial for the treatment of deep tissues.<sup>21,22</sup> As for PDT, photosensitizers such as porphyrin, phthalocyanines, and bacteriochlorin derivatives

<sup>a</sup>College of Pharmacy, School of Basic Medicine, Ningxia Medical University, Yinchuan, Ningxia 750004, China. E-mail: huiqin\_yao@163.com

<sup>b</sup>CAS Key Laboratory for Biomedical Effects of Nanomaterials and Nanosafety, Institute of High Energy Physics, National Center for Nanoscience and Technology, Chinese Academy of Sciences, Beijing 100049, China. E-mail: zuyan@ihep.ac.cn; yinwy@ihep.ac.cn

† Electronic supplementary information (ESI) available. See DOI: 10.1039/d2ra00963c

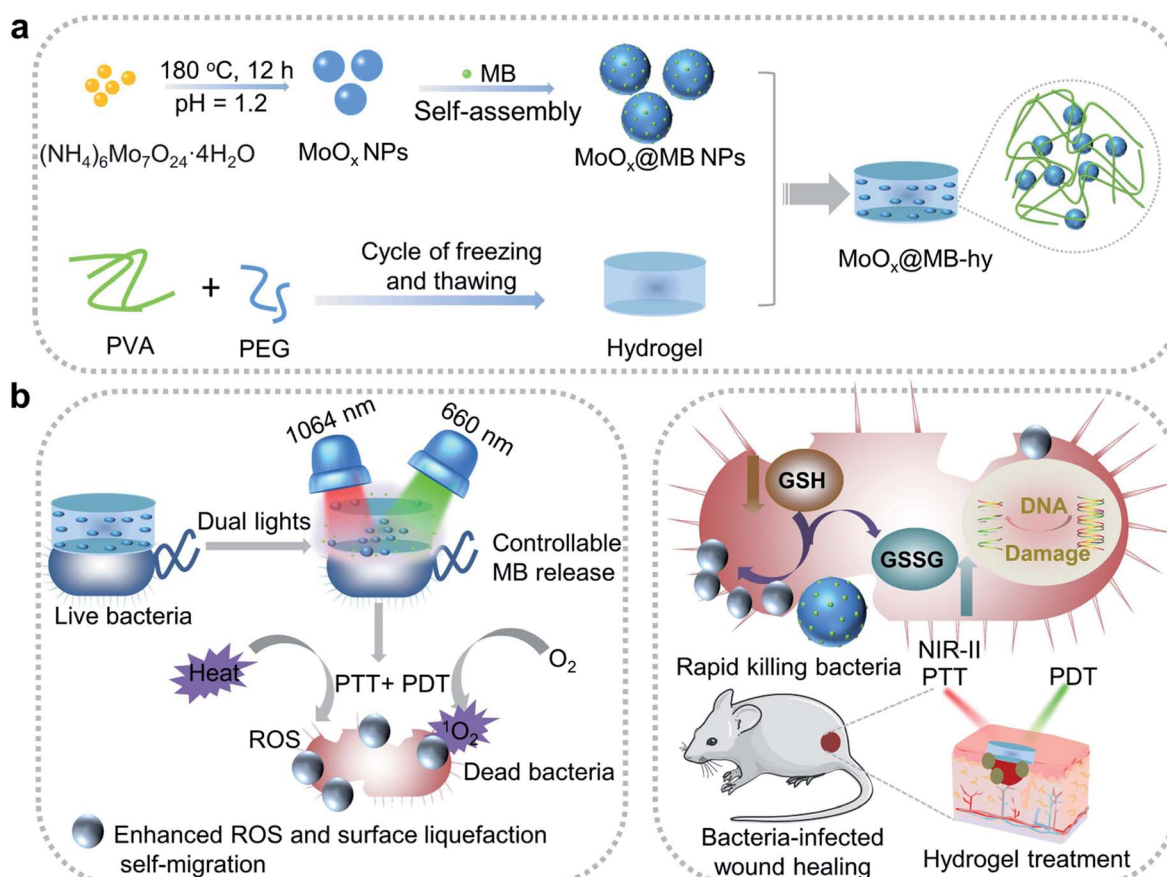


are exposed to visible light to produce singlet oxygen ( ${}^1\text{O}_2$ ), leading to local bacterial death.<sup>23</sup> The efficient delivery of photosensitizers to the infection site for a better killing effect has aroused great concern.<sup>24</sup> Among these photosensitizers, methylene blue (MB), which has been used clinically,<sup>25,26</sup> can effectively treat bacterial infection based on PDT. Nano-materials loaded with MB have been reported to treat bacterial-infection diseases with effective PDT.<sup>27-29</sup> However, there are still some questions based on these phototherapeutic strategies: (I) directly adding the photosensitizer or photothermal agent into the wound site may induce superfluous concentrations of them and cytotoxicity, consequently reducing the wound healing effect; (II) high-power photothermal treatment alone has certain side effects on normal tissues around wounds, while reactive oxygen species (ROS) in PDT have a short lifespan (<3.5  $\mu\text{s}$ ), short diffusion distances (tens to hundreds of nanometers) and are usually non-selective.<sup>30,31</sup> Fortunately, the emergence of hydrogel-based combination therapy offers hope for solving these problems. After combining with hydrogels, the accurate delivery of intelligent nanomaterials, such as photothermal nanoagents and/or a photosensitizer, to the wound site is easily achieved.

Up to now, researchers have shown increasing interest in the study of hydrogels as a scaffold for the delivery of local

antibacterial drugs and nanomaterials to effectively treat wound infection.<sup>33</sup> The hydrogels can act as a barrier to isolate micro-organisms, providing some relief from pain. In addition, its natural porous structure can not only absorb tissue fluid from the wound, and maintain good water and oxygen permeability, but can also promote the dispersion and stability of nano-materials.<sup>34,35</sup> Some hydrogels have been widely utilized clinically. At present, in the market, a very common function of hydrogels product is hemostatic, where it is superior to gauze and bandage.<sup>36</sup> In addition, specific hydrogels can also be used to overcome the problem of short ROS lifespan, so that the utilization rate of ROS is significantly improved.<sup>32</sup> Nowadays, a typical poly(vinyl alcohol) (PVA) polymer, with good water solubility and biocompatibility, can also be used to construct biomedical hydrogels in the clinic.<sup>37</sup> Polyethylene glycol (PEG) with good biocompatibility and low immunogenicity has also been used in the biomedical field.<sup>38</sup> Compared with pure PVA hydrogel, the biocompatible PVA/PEG hybrid can form hydrogels with increased mechanical strength, high elasticity and lubrication for biomedical applications.<sup>39-41</sup>

In this work, we designed a biocompatible  $\text{MoO}_x@\text{MB}$ -incorporated PVA/PEG nanocomposite hydrogel ( $\text{MoO}_x@\text{MB-hy}$ ) with outstanding light-activated antibacterial activity. The  $\text{MoO}_x@\text{MB}$  NPs were synthesized by a simple self-assembly



**Scheme 1** Schematic illustration of (a) the synthesis of the  $\text{MoO}_x@\text{MB-hy}$  dressing and (b) dual lights synergistic PTT-PDT activated strategy induced ROS enhancement and surface self-migration to rapidly promote bacterial eradication and wound healing.

strategy and then incorporated into the porous PVA/PEG hydrogel to achieve good dispersion (Scheme 1a). Due to the high NIR-II photothermal conversion efficiency of  $\text{MoO}_x$ , the photosensitizer MB can achieve the most controllable release from  $\text{MoO}_x@\text{MB-hy}$ . Subsequently, under mild 660 nm laser irradiation,  $\text{MoO}_x@\text{MB-hy}$  effectively produces more singlet oxygen ( ${}^1\text{O}_2$ ). Simultaneously,  $\text{MoO}_x@\text{MB-hy}$  traps the bacteria to the distance limit of ROS damage to achieve a surface-liquefaction self-migration effect on the bacteria, enormously overcoming the intrinsic shortcomings of short diffusion distance and lifetime of ROS (Scheme 1b). The safety of  $\text{MoO}_x@\text{MB-hy}$  is high, and this ROS-enhanced dual-phototherapy has a significant curative effect. Due to the synergistic effect of PTT and PDT,  $\text{MoO}_x@\text{MB-hy}$  can break the glutathione (GSH) antioxidant balance and achieve enhanced ROS accumulation to rapidly eradicate both ampicillin-resistant *Escherichia coli* (Amp<sup>r</sup> *E. coli*) and *Bacillus subtilis* (*B. subtilis*) under dual-light irradiation within 15 min. The heat and ROS induced by PTT and PDT enhance bacterial membrane permeability, and then more ROS can easily enter the membrane of the bacteria quickly, improving the bactericidal effect. The biodegradable  $\text{MoO}_x$  NPs can not only reduce the wound burden when a small amount of them remain on the wound but can also be beneficial to medical waste disposal. The dual-light-activated  $\text{MoO}_x@\text{MB-hy}$  also accelerates the healing of wounds infected with Amp<sup>r</sup> *E. coli* in mice. This strategy opens a new avenue to fabricate hydrogel dressings with rapid sterilization and wound healing.

## 2. Experimental section

### 2.1 Materials

Ethanol ( $\text{C}_2\text{H}_5\text{OH}$ ) and hydrochloric acid (HCl) were purchased from Beijing Chemical Corporation (Beijing, China). Polyethylene glycol (PEG, Mw = 4000) and ammonium molybdate tetrahydrate  $[(\text{NH}_4)_6\text{Mo}_7\text{O}_{24} \cdot 4\text{H}_2\text{O}]$  were purchased from Aladdin Co. Ltd. Dulbecco's penicillin-streptomycin solution, fetal bovine serum (FBS) and Dulbecco's modified eagle medium (DMEM) were purchased from Gibco (Shanghai, China). A Cell Counting Kit-8 assay (CCK-8) was purchased from Beijing Solarbio Science & Technology Co., Ltd. Poly(vinyl alcohol) (PVA) (Mw = 146 000–186 000) was obtained from Acros. Methylene blue (MB) was obtained from Alfa Aesar. All chemicals were of research grade and were used without further purification. The deionized (DI) water used in the experiment was obtained from an 18 M $\Omega$  (SHRO-plus DI) system.

### 2.2 Synthesis of nanocomposite hydrogels

**2.2.1 Synthesis of  $\text{MoO}_x@\text{MB}$  NPs.** The  $\text{MoO}_x$  NPs were synthesized according to the procedure described in our previous report.<sup>19</sup> First, 0.0865 g of  $(\text{NH}_4)_6\text{Mo}_7\text{O}_{24} \cdot 4\text{H}_2\text{O}$  was dissolved into a 30 mL water/ethanol mixture (volume ratio of water to ethanol = 2 : 1) under stirring. Second, the pH of the mixed solution was modulated to 1.2 with HCl. Then, the mixed solution was transferred to a Teflon-lined autoclave and then heated at 180 °C for 12 h. After the reaction, the precipitate was

washed with deionized water three times and collected by centrifugation. Finally, the obtained samples were freeze-dried for further use.  $\text{MoO}_x@\text{MB}$  NPs were prepared by a simple self-assembly strategy based on electrostatic interaction. Typically, MB (0.2 mg mL<sup>-1</sup>) and  $\text{MoO}_x$  NPs (1 mg mL<sup>-1</sup>) were mixed in deionized water for 12 h at room temperature. Then, the  $\text{MoO}_x@\text{MB}$  NPs were washed three times, collected by centrifugation and freeze-dried.

**2.2.2 Synthesis of PVA/PEG hydrogel.** The PVA/PEG hydrogel was synthesized according to a previously described method with minor modification.<sup>40,41</sup> 1.5 g of PVA and 0.9 g of PEG were dissolved in 14 mL of DI water and maintained at 90 °C for 40 min. Then, the mixture became a homogenous viscous solution. Next, the solution was frozen at –20 °C for 4 h, then thawed at 20 °C for 4 h. Several freezing–thawing cycles were implemented and three-dimensional porous hydrogels were formed.

**2.2.3 Synthesis of  $\text{MoO}_x@\text{MB-hy}$ .** 1 mL of the above PVA/PEG solution was put in one well of a 48-well plate, and 250 µg of  $\text{MoO}_x@\text{MB}$  NPs were added to the well to synthesize 250 µg mL<sup>-1</sup>  $\text{MoO}_x@\text{MB}$ -incorporated hydrogels ( $\text{MoO}_x@\text{MB-hy}$ ). The mixed solution was stirred for 20 min and frozen at –20 °C for 4 h, then thawed at 20 °C for 4 h. Several freezing–thawing cycles were implemented and three-dimensional porous  $\text{MoO}_x@\text{MB-hy}$  was formed. In addition,  $\text{MoO}_x@\text{MB-hy}$  with different nanomaterial concentrations or  $\text{MoO}_x$ -incorporated hydrogels were prepared in a similar way. In this study, unless otherwise specified, hydrogels with the nanomaterial concentration 250 µg mL<sup>-1</sup> were used in most experiments. The obtained cylindrical hydrogels were cut into tablets with a diameter of 8 mm and a height of 2 mm for further use.

### 2.3 Characterization

The microstructure and morphology of the as-prepared samples were investigated by transmission electron microscopy (TEM, JEM 2100 Plus, JEOL) and field-emission scanning electron microscopy (FE-SEM, Hitachi S-4800), respectively. The phase and crystallography of the materials were measured using X-ray powder diffraction (XRD) analysis on a Bruker D8 Advance diffractometer with Cu-K $\alpha$  radiation ( $\lambda = 1.5418 \text{ \AA}$ ). X-ray photoelectron spectroscopy (XPS) was obtained with a spectrometer (ESCALab250i-XL) using monochromatic Al-K $\alpha$  radiation (1486.6 eV). The hydrodynamic size and zeta potential of the materials were detected with a DLS particle size analyzer (Brookhaven Omni). Ultraviolet-visible-near-infrared (UV-Vis-NIR) spectra were characterized with a Hitachi U-3900 spectrophotometer. Thermogravimetric analysis (TGA, Q50) was performed to check the disintegration of the samples at diverse temperatures (0–900 °C). The mechanical properties of the samples were investigated with a microcomputer-controlled electronic universal testing machine (RGM-6005T, Reger Experimental Instrument Co. Ltd, China) at room temperature.

### 2.4 Loading capacity of MB

The loading capacity of MB by  $\text{MoO}_x$  NPs was measured by the reported method with slight modifications.<sup>42</sup> 2 mg of



$\text{MoO}_x@\text{MB}$  NPs and 2 mL of absolute ethanol were mixed and then vortexed for 5 min to accelerate the release of MB. Then, to collect the released MB, the mixture was centrifuged at 12 000 rpm for 20 min. Finally, the absorbance of MB in the supernatant solution was detected spectrophotometrically at 660 nm. The loading capacity was expressed as the amount of MB ( $\mu\text{g}$ ) bound per mg of  $\text{MoO}_x$  NPs.

## 2.5 Compression and swelling behavior test

The mechanical properties of the pure hydrogel and  $\text{MoO}_x@\text{MB}$ -hy were investigated with a microcomputer-controlled electronic universal testing machine. The sample had a diameter of 8 mm and a height of 14 mm. The compression tests were at a speed of  $2 \text{ mm min}^{-1}$ .

To evaluate the swelling properties, the hydrogels were first freeze-dried and then the weights were recorded. Next, the dry hydrogels were immersed in phosphate buffered saline (PBS) solution at  $37^\circ\text{C}$  and the weights were collected at different time points. The swelling ratios ( $S$ ) of the hydrogels were determined using the following equation:  $S = (W_t - W_0)/W_0 \times 100\%$ , where  $W_0$  is the weight of dried hydrogel and  $W_t$  is the weight of the hydrogel at different time points.

## 2.6 pH-dependent degradation of $\text{MoO}_x@\text{MB}$ NPs

After the  $\text{MoO}_x$  and  $\text{MoO}_x@\text{MB}$  NPs were dispersed in two pH buffer solutions (10 mM citrate buffer at pH 5.5 and 10 mM PBS at 7.4), changes in their morphologies and size were monitored at various time points by a camera and TEM. As for the degradation behavior of the NPs on the hydrogels, the morphologies of the nanocomposite hydrogels were captured by a camera.

## 2.7 Photothermal effects

In order to evaluate the photothermal effect of the hydrogel nanocomposites loaded with various concentrations of  $\text{MoO}_x@\text{MB}$  NPs (50, 100, 250 and 500  $\mu\text{g mL}^{-1}$ ), 1064 nm laser irradiation at a power density of  $0.5 \text{ W cm}^{-2}$  was focused onto a spot on  $\text{MoO}_x@\text{MB}$ -hy with 0.3 mL of PBS. The pure hydrogel was used as a control. Each  $\text{MoO}_x@\text{MB}$ -hy was irradiated for 10 min.  $\text{MoO}_x@\text{MB}$ -hy was also irradiated by a 1064 nm laser with different power densities ( $0.3, 0.4, 0.5$  and  $0.6 \text{ W cm}^{-2}$ ). To investigate the photothermal stability,  $\text{MoO}_x@\text{MB}$ -hy containing 250  $\mu\text{g mL}^{-1}$   $\text{MoO}_x@\text{MB}$  with 0.3 mL of PBS was treated with five repeated 10 min-on/off laser cycles with 1064 nm irradiation ( $0.5 \text{ W cm}^{-2}$ ). The real-time temperature of the hydrogels was recorded by a thermal camera (FLIR Therma CAM E40).

## 2.8 Photothermal stability tests of hydrogels in the blocking setup

Hydrogels were placed in the neck of glass Pasteur pipettes.<sup>43</sup> Then, water (500  $\mu\text{L}$ ) was poured on top of the hydrogels. Then, the 1064 nm laser horizontally illuminated the hydrogel in the glass Pasteur pipettes. The pipettes were kept at  $25^\circ\text{C}$  (without the laser) or irradiated by the 1064 nm laser ( $0.5 \text{ W cm}^{-2}$ ). Photographs were taken to monitor the changes at different time points (0 s, 20 s and 50 s). Pipettes containing hydrogels at

$37^\circ\text{C}$  were also investigated for 24 h and 48 h for possible changes. The temperature changes in the hydrogels in the pipettes were also monitored by an FLIR photothermal camera.

## 2.9 *In vitro* release of MB and Mo ions from $\text{MoO}_x@\text{MB}$ -hy

The release behaviors of MB and Mo ions from  $\text{MoO}_x@\text{MB}$ -hy were also investigated. First, 1 mL of PBS solution was added to a 24-well plate containing  $\text{MoO}_x@\text{MB}$ -hy. Then,  $\text{MoO}_x@\text{MB}$ -hy was irradiated under a 1064 nm laser ( $0.5 \text{ W cm}^{-2}$ ) for 10 min followed by an interval of 30 min.  $\text{MoO}_x@\text{MB}$ -hy without 1064 nm laser irradiation was set as a control. The on-off irradiation cycle was repeated three times. The concentration of released MB from  $\text{MoO}_x@\text{MB}$ -hy was calculated by recording the absorbance of the supernatant in the 24-well plate at 660 nm using UV-Vis spectroscopy. Meanwhile, the amount of Mo ions released from  $\text{MoO}_x@\text{MB}$ -hy was quantified by inductively coupled plasma-mass spectrometry (ICP-MS).

## 2.10 Singlet oxygen detection *in vitro*

The singlet oxygen ( ${}^1\text{O}_2$ ) measurements were carried out with a fluorescence spectrophotometer and singlet oxygen sensor green (SOSG) was used as an indicator to determine the amount of  ${}^1\text{O}_2$ . SOSG is a commercially available fluorescent dye, which has a high specificity towards  ${}^1\text{O}_2$  and no affinity for the other ROS. 3 mL of SOSG (final concentration of 2.5  $\mu\text{M}$ ) aqueous solutions were incubated with  $\text{MoO}_x@\text{MB}$  NPs,  $\text{MoO}_x@\text{MB}$  NPs (660 nm),  $\text{MoO}_x@\text{MB}$  NPs (1064 nm) and  $\text{MoO}_x@\text{MB}$  NPs (dual lights), respectively. The solution containing only SOSG was set as a control. The final concentration of  $\text{MoO}_x@\text{MB}$  NPs was 50  $\mu\text{g mL}^{-1}$ . The 1064 nm laser irradiation was conducted at  $0.5 \text{ W cm}^{-2}$  for 10 min and the 660 nm laser irradiation was performed at  $100 \text{ mW cm}^{-2}$  for 5 min. The dual-light irradiation was successive irradiation by a 1064 nm laser for 10 min and by a 660 nm laser for 5 min. Afterward, the supernatants were collected by centrifugation. The fluorescence intensity was quantitatively recorded at 531 nm with an excitation wavelength of 488 nm by a fluorescence spectrophotometer (Horiba FluoroLog-3, Japan). To detect the  ${}^1\text{O}_2$  produced by the hydrogels, the hydrogels were immersed in SOSG solution and the experiments performed with different treatments, including pure hydrogel,  $\text{MoO}_x@\text{MB}$ -hy,  $\text{MoO}_x@\text{MB}$ -hy (660 nm),  $\text{MoO}_x@\text{MB}$ -hy (1064 nm) and  $\text{MoO}_x@\text{MB}$ -hy (dual lights). Finally, the fluorescence intensities of the SOSG solutions were measured as described as above.

## 2.11 GSH depletion

GSH depletion can be assessed using Ellman reagent 5,5'-dithiobis(2-nitrobenzoic acid) (DTNB). DTNB can cleave the disulfide bonds ( $-\text{S}-\text{S}-$ ) and the resultant yellow product is 2-nitro-5-thiobenzoate acid. Briefly, pure hydrogel and  $\text{MoO}_x@\text{MB}$ -hy were respectively immersed in bicarbonate buffer solutions containing GSH (0.8 mM, 300  $\mu\text{L}$ ). The solution containing only GSH was set as a control. Each  $\text{MoO}_x@\text{MB}$ -hy group respectively performed with different treatments including  $\text{MoO}_x@\text{MB}$ -hy,  $\text{MoO}_x@\text{MB}$ -hy (660 nm),  $\text{MoO}_x@\text{MB}$ -hy (1064 nm) and  $\text{MoO}_x@\text{MB}$ -hy (dual lights). Then, the



differently treated GSH solutions were respectively mixed with Tris-HCl (pH = 8) solution (0.05 M, 2.4 mL) and DTNB (0.1 M, 45  $\mu$ L). The absorbance of the above mixtures at 410 nm was recorded with a microplate spectrophotometer (SpectraMax M2MDC, USA).

## 2.12 Cell culture and cytotoxicity assay

Mouse embryonic fibroblast cell line (NIH3T3) and human umbilical vein endothelial cells (HUVEC) were grown in complete medium (DMEM medium + 10% FBS + 1% penicillin-streptomycin solution) at 37 °C under 5% CO<sub>2</sub>.

The cytotoxicity of MoO<sub>x</sub>@MB NPs to NIH3T3 and HUVEC cells was investigated using a cell counting kit (CCK-8) assay. NIH3T3 or HUVEC cells were respectively added into a 96-well plate at a density of  $8 \times 10^3$  cells per well and grown in complete medium for 24 h. Next, the culture medium was taken out and the cells were incubated with MoO<sub>x</sub>@MB NPs at concentrations of 10, 20, 40, 60, 80 and 100  $\mu$ g mL<sup>-1</sup>. After another 24 h of incubation, 10% CCK-8 solutions were added. The cell viability was evaluated by monitoring the absorbance at 450 nm with a microplate spectrophotometer.

The *in vitro* cytotoxicity of the hydrogels was also evaluated by the CCK-8 method using the hydrogel extracts. MoO<sub>x</sub>@MB-hy with different concentrations of MoO<sub>x</sub>@MB NPs (50, 100, 250 and 350  $\mu$ g mL<sup>-1</sup>) were prepared. The hydrogels were severally soaked in 1 mL of complete medium at 37 °C for 24 h to acquire the hydrogel extracts. NIH3T3 cells or HUVEC cells were placed in 48-well plates at a density of  $15 \times 10^3$  cells per well. After 24 h of incubation, the cells were incubated with various concentrations of hydrogel extracts and co-incubated for another 24 h or 48 h. Then, the hydrogel extracts were sucked out of the 48-well plates and 10% CCK-8 solutions were added. The supernatants were taken and the absorbance at 450 nm was read with a microplate spectrophotometer.

## 2.13 In vitro hemolysis test

To assess the blood compatibility of the hydrogels, a hemolysis assay was employed. The fresh blood of healthy female BALB/c mice was first obtained, and then we collected the red blood cells (RBCs) by centrifugation (2000 rpm, 10 min). Pure hydrogel and MoO<sub>x</sub>@MB-hy (250  $\mu$ g mL<sup>-1</sup>) were incubated with the RBCs at 37 °C for 60 min.<sup>44</sup> Then, PBS (negative control) and distilled water (positive control), respectively, were added to the RBCs. After centrifugation, photographs of the tubes were taken. Finally, the supernatant absorbance of all samples at 541 nm was determined by UV-Vis spectroscopy.

## 2.14 Antibacterial assays

**2.14.1 Bacterial culture and *in vitro* antibacterial experiments.** Gram-negative ampicillin-resistant *Escherichia coli* (Amp<sup>r</sup> *E. coli*) and Gram-positive *B. subtilis* were used as two model microorganisms. Amp<sup>r</sup> *E. coli* cultured on solid Luria-Bertani (LB) agar plates were transferred to 10 mL of LB broth with ampicillin (50  $\mu$ g mL<sup>-1</sup>). Gram-positive *B. subtilis* cultured on solid LB agar plates were added to 10 mL of LB broth. Then, the bacterial solutions were shaken at 150 rpm and 37 °C for

12 h and the bacteria were gathered by centrifugation at 4000 rpm for 5 min. Then, the collected bacteria were washed three times with PBS. Finally, the bacteria were diluted with PBS to an optical density (OD<sub>600</sub> = 0.1, with equivalent  $1.0 \times 10^8$  CFU mL<sup>-1</sup>) at 600 nm.

The antibacterial properties of MoO<sub>x</sub>@MB-hy (250  $\mu$ g mL<sup>-1</sup>) were then evaluated by the plate counting method, and four groups were set: (1) control (only bacteria), (2) bacteria + pure hydrogel, (3) bacteria + MoO<sub>x</sub>-hy and (4) bacteria + MoO<sub>x</sub>@MB-hy. Before the experiment, all the hydrogels were soaked in 75% alcohol for 20–30 min for disinfection and then washed with PBS three times. The bacterial suspensions (1.0  $\times 10^7$  CFU mL<sup>-1</sup>, 0.3 mL) in PBS were respectively added to 48-well plates containing pure hydrogel, MoO<sub>x</sub>-hy and MoO<sub>x</sub>@MB-hy. The control group contained only bacteria. Next, each group was respectively subjected to four kinds of treatments: dark conditions, 660 nm (100 mW cm<sup>-2</sup>, 5 min), 1064 nm (0.5 W cm<sup>-2</sup>, 10 min) and dual lights. After different laser treatments, the bacterial solutions were collected and diluted 1000 times with PBS. The diluted bacterial solutions (100  $\mu$ L) were placed in solid LB agar plates, which were then kept at 37 °C for 12 h. The bacteria colonies on the solid LB agar plates were counted and photographed.

**2.14.2 Morphology observation of bacteria.** Morphology changes of bacteria treated with PBS, pure hydrogel and MoO<sub>x</sub>@MB-hy with laser irradiation were observed by FE-SEM images. First, the bacterial suspensions were fixed with paraformaldehyde (4%) for 6 h. Then, the bacteria were dehydrated for 10 min in different volume percentages of ethanol (30%, 50%, 70%, 80%, 90% and 100%). Finally, the bacterial suspensions were diluted appropriately, dropped onto a silicon wafer, and observed.

**2.14.3 Live/dead bacterial cell staining.** SYTO-9 and propidium iodide (PI) were utilized to label living and dead bacterial cells. Bacteria were treated with PBS, pure hydrogel and MoO<sub>x</sub>@MB-hy with laser irradiation. Then, the treated bacteria in each group were further treated with SYTO-9 and PI for 30 min. After staining, PBS was used to wash the treated bacterial suspensions three times and remove excess SYTO-9 and PI. Finally, the bacteria were dispersed in 30  $\mu$ L of PBS and 10  $\mu$ L of bacterial suspension was added on the surface of the slides for 2 min. Images of stained bacteria were taken by confocal fluorescence microscopy.

## 2.15 In vivo wound healing assay

The animals used in this experiment were female BALB/c mice (six–eight weeks old). The mice were randomly divided into six groups: PBS, kanamycin (Kana), pure hydrogel, MoO<sub>x</sub>@MB-hy (660 nm), MoO<sub>x</sub>@MB-hy (1064 nm) and MoO<sub>x</sub>@MB-hy (dual lights). There were nine mice in each group. After shaving, all the mice in these groups had a round wound with a diameter of 5 mm cut on the back skin. Afterwards, Amp<sup>r</sup> *E. coli* suspensions (10<sup>8</sup> CFU mL<sup>-1</sup>, 10  $\mu$ L) were added to the wounds. After 24 h, the wounds of the mice were treated with PBS (10  $\mu$ L), Kana (8  $\mu$ g mL<sup>-1</sup>, 10  $\mu$ L),<sup>45</sup> pure hydrogel, MoO<sub>x</sub>@MB-hy + 660 nm, MoO<sub>x</sub>@MB-hy + 1064 nm and MoO<sub>x</sub>@MB-hy (dual lights). PBS



and Kana solutions were directly dripped onto the wounds of the mice. For the pure hydrogel treated group, the pure hydrogel only stayed on the wound for 15 min without any irradiation. The duration time of the pure hydrogel group is consistent with the groups with dual-light irradiation time (15 min). And the 1064 nm laser irradiation for  $\text{MoO}_x@\text{MB-hy}$  ( $250 \mu\text{g mL}^{-1}$ ) covering the wound was  $0.3 \text{ W cm}^{-2}$  for 10 min, while the 660 nm laser irradiation was  $100 \text{ mW cm}^{-2}$  for 5 min. As for the dual-light irradiation, the wounds were first irradiated with 1064 nm at  $0.3 \text{ W cm}^{-2}$  for 10 min and then irradiated with 660 nm at  $100 \text{ mW cm}^{-2}$  for 5 min. The temperature changes of the wounds during the *in vivo* therapy were monitored with an FLIR photothermal camera. On day 2 after the treatment, the wound tissues were separated and homogenized in PBS (2 mL). Next, the solutions containing bacteria were diluted 10 times. Finally,  $100 \mu\text{L}$  of the diluted solutions were added onto solid LB medium by the spread plate method. The growth of bacterial colonies was determined for quantitative analysis. Relative bacteria number = CFU (test group)/CFU (control group)  $\times$  100%. Digital images of the wound were taken using a COOLPIX P900S camera on days 0, 6 and 10. Mouse weights were monitored over time.

On day 10, blood samples from the healthy mice group (without wounds) and  $\text{MoO}_x@\text{MB-hy}$  (dual lights) group were obtained from the fundus artery of the mice.  $100 \mu\text{L}$  of blood sample was mixed with EDTA (anticoagulant) for routine blood analysis indexes. 1 mL of blood stood at  $4^\circ\text{C}$  for 2 h and was centrifuged. The obtained serum was then used in biochemical testing. All animal operations were carried out according to the guidelines for the Care and Use of Experimental Animals by the National Nanotechnology Center and approved by the Animal Ethics Committee of the National Nanotechnology Center of the Chinese Academy of Sciences.

Wound tissues were also evaluated by hematoxylin and eosin (H&E) and Masson's trichrome staining. Typically, the wound tissues on day 2 and day 10 were also harvested and fixed with 4% formaldehyde solution. Main organs like heart, liver, spleen, lung and kidney were taken from the mice and fixed in formalin solution. Then H&E staining and histological examination were conducted. The pathological section images were captured with an inverted fluorescence microscope for *in vivo* biosafety evaluation.

## 2.16 Statistical analysis

The obtained experimental data were expressed as mean  $\pm$  standard deviation (SD). A Student's *t*-test was performed ( $*p < 0.05$ , significant;  $**p < 0.01$ , moderately significant;  $***p < 0.001$ , highly significant).

## 3. Results and discussion

### 3.1 Synthesis and characterization of $\text{MoO}_x@\text{MB NPs}$

$\text{MoO}_x$  NPs were first synthesized according to our previous report with minor modification.<sup>19</sup> Then, the  $\text{MoO}_x@\text{MB}$  NPs were prepared by a simple electrostatic self-assembly strategy of mixing  $\text{MoO}_x$  NPs with methylene blue (MB) under stirring for 12 h.

The  $\text{MoO}_x@\text{MB}$  can be observed in the transmission electron microscopy (TEM) image as NPs with a diameter of 20–30 nm (Fig. 1a), similar to  $\text{MoO}_x$  NPs (Fig. S1a†). The high-resolution transmission electron microscopy (HR-TEM) image indicates both  $\text{MoO}_x$  NPs and  $\text{MoO}_x@\text{MB}$  NPs with an interplanar spacing of about 0.34 nm (Fig. S1b† and 1b), corresponding to the (−111) lattice plane of monoclinic phase  $\text{MoO}_2$ .<sup>46</sup> Both the  $\text{MoO}_x$  NPs and  $\text{MoO}_x@\text{MB}$  NPs are dark blue with good dispersion in aqueous solution (Fig. S1c† and 1c). In addition, dynamic light scattering (DLS) measurements show that both the hydrodynamic diameters of  $\text{MoO}_x$  NPs and  $\text{MoO}_x@\text{MB}$  NPs in distilled water are about 50 nm (Fig. S1d† and 1d). The zeta potential of  $\text{MoO}_x$  NPs is  $-15.04 \pm 1.00 \text{ mV}$ , while the zeta potential changes to  $-7.65 \pm 1.62 \text{ mV}$  after the self-assembly of MB to the  $\text{MoO}_x$  surface through electrostatic interaction (Fig. 1e). As MB is a promising photosensitizer applied in the PDT, the loading capacity of MB by  $\text{MoO}_x$  NPs was calculated to be  $3.04 \mu\text{g}$  of MB adsorption per mg of  $\text{MoO}_x$  NPs. The crystal structures of the  $\text{MoO}_x$  NPs and  $\text{MoO}_x@\text{MB}$  NPs were manifested by X-ray diffraction (XRD) patterns (Fig. 1f), which can be fitted well with two combined phase structures of orthorhombic  $\text{Mo}_4\text{O}_{11}$  phase (JCPDS 65-0397) and monoclinic  $\text{MoO}_2$  phase (JCPDS 65-1273).<sup>16,19</sup> Moreover, the inductively coupled plasma-mass spectrometry (ICP-MS) results give an atomic ratio of Mo/O in  $\text{MoO}_x$  of approximately 1 : 2.18. The chemical states of the elements in  $\text{MoO}_x@\text{MB}$  NPs were revealed by X-ray photoelectron spectroscopy (XPS). The full spectrum shows the presence of Mo, C, and O of  $\text{MoO}_x@\text{MB}$  NPs (Fig. 1g). The N 1s curve of  $\text{MoO}_x@\text{MB}$  NPs is shown in Fig. S2,† indicating the presence of MB. The Mo 3d XPS spectrum of  $\text{MoO}_x@\text{MB}$  NPs can be fitted into six peaks, assigned to  $\text{Mo}^{4+}$  (228.74 and 231.93 eV),<sup>47</sup>  $\text{Mo}^{5+}$  (230.34 and 233.724 eV)<sup>48</sup> and  $\text{Mo}^{6+}$  (231.80 and 235.17 eV)<sup>49</sup> (Fig. 1h). The XPS result proves the mixed valence states of Mo on the surface of  $\text{MoO}_x@\text{MB}$  NPs due to oxygen vacancies, which is also the main reason for the NIR-II absorption of this nanomaterial.<sup>19</sup> The UV-Vis-NIR absorbance of  $\text{MoO}_x$  NPs (Fig. S3†) and  $\text{MoO}_x@\text{MB}$  NPs are also displayed (Fig. 1i). In addition, the wide NIR absorption from 700 nm to 1200 nm, and the obvious absorbance at 660 nm of  $\text{MoO}_x@\text{MB}$  NPs can be observed, which is associated with the inherent absorbance of MB.

### 3.2 Synthesis and characterization of $\text{MoO}_x@\text{MB-hy}$

Hydrogels were prepared based on polyvinyl alcohol (PVA) and polyethylene glycol (PEG) *via* polymer blending. 3D porous hydrogels were formed through several freezing–thawing cycles. The synthetic processes of the hydrogels are illustrated in Fig. S4a,† The morphologies of the pure hydrogel and  $\text{MoO}_x@\text{MB-hy}$  can be given by field-emission scanning electron microscopy (FE-SEM). The porous 3D network structure can be observed in the pure hydrogel. This porous structure is favorable for nutrition transport, and gas and water exchange (Fig. 2a). As shown in Fig. 2b, the pore size of  $\text{MoO}_x@\text{MB-hy}$  is smaller than that of pure hydrogel, and it still exhibited a 3D network structure. This may be due to the  $\text{MoO}_x@\text{MB}$  NPs having partly filled in some of the pore structures, making the hydrogel pore narrower. Furthermore, the photographs of the



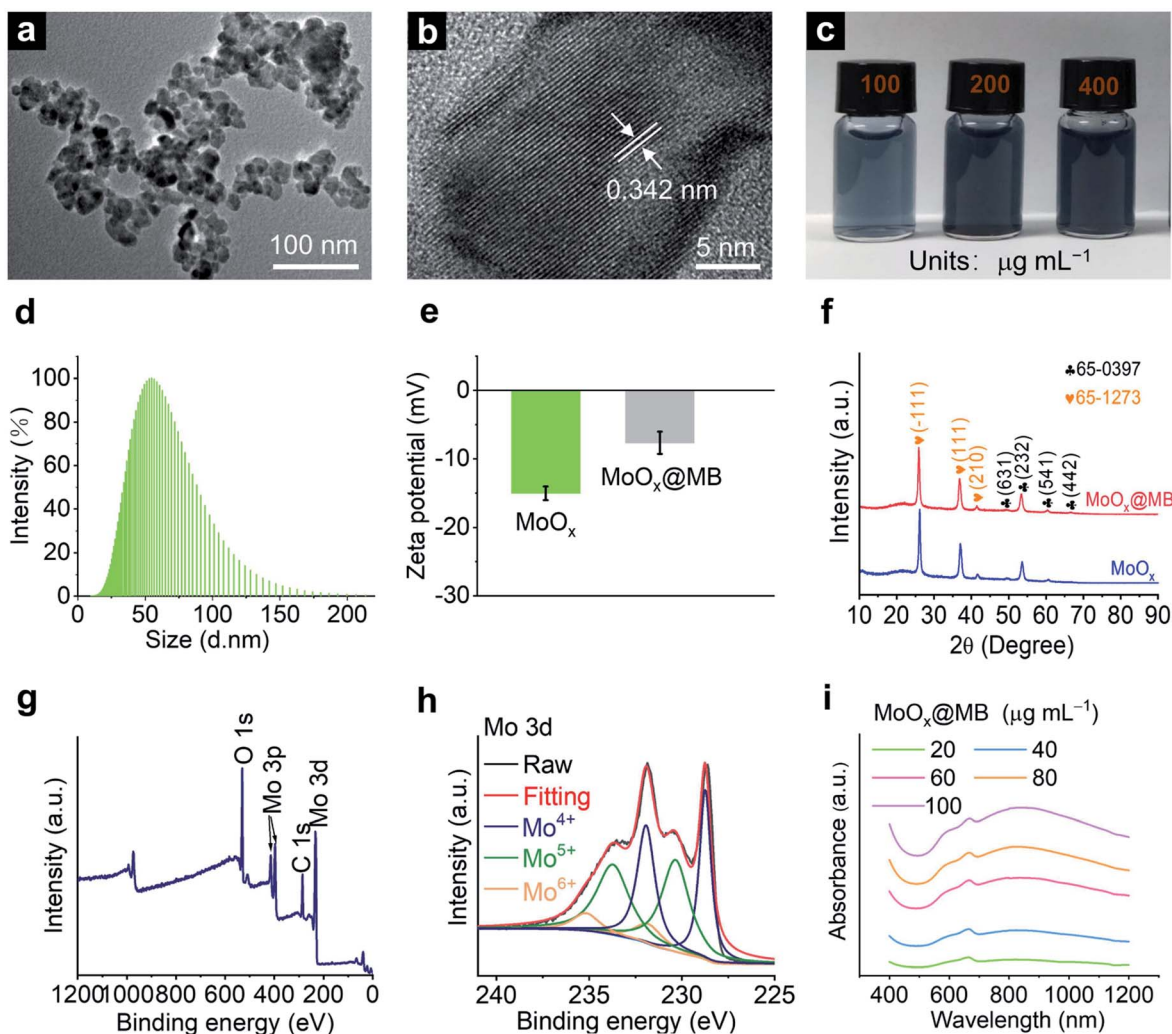


**Fig. 1** (a) TEM and (b) HR-TEM images of  $\text{MoO}_x$ @MB NPs. (c) Digital images of  $\text{MoO}_x$ @MB NPs solutions with different concentrations. (d) DLS pattern of  $\text{MoO}_x$ @MB NPs. (e) Zeta potential of  $\text{MoO}_x$  and  $\text{MoO}_x$ @MB NPs. (f) XRD patterns of  $\text{MoO}_x$  and  $\text{MoO}_x$ @MB NPs. (g) A full XPS survey spectrum and (h) Mo 3d core level spectrum of  $\text{MoO}_x$ @MB NPs. (i) UV-Vis-NIR absorption spectra of  $\text{MoO}_x$ @MB solutions with different concentrations.

pure hydrogel,  $\text{MoO}_x$ -hy and  $\text{MoO}_x$ @MB-hy dressings in Fig. 2c indicate their shapes and colors. After introducing  $\text{MoO}_x$  or  $\text{MoO}_x$ @MB NPs, the colors of the suspensions and hydrogels change from white to dark blue, indicating the uniform loading of NPs into the hydrogels.

### 3.3 Swelling behavior, mechanical properties and degradation behaviors

The hydrogel dressings provide a moist environment for wounds and can absorb secretions from the wound or infection sites. The swelling capacity reflects the water absorption capacity of the hydrogel. Thus, the swelling abilities of pure hydrogel,  $\text{MoO}_x$ -hy and  $\text{MoO}_x$ @MB-hy were measured (Fig. 2d). All the hydrogels can reach water saturation within 50 min. The equilibrated swelling ratios (ESR) of pure hydrogel,  $\text{MoO}_x$ -hy and  $\text{MoO}_x$ @MB-hy are 648.40%, 605.52% and 596.11%, respectively. The pure hydrogel possesses better swelling capacity than  $\text{MoO}_x$ -hy or  $\text{MoO}_x$ @MB-hy. This may be due to the

$\text{MoO}_x$  and  $\text{MoO}_x$ @MB NPs in the network structure causing a certain degree of hindrance to water entering the hydrogel grid.

Some literature has reported that the addition of nanomaterials, such as GO<sup>50</sup> and ZnO NPs,<sup>51</sup> can greatly improve the mechanical properties of PVA hydrogels. To evaluate the impact of  $\text{MoO}_x$ @MB NPs on the mechanical properties of the PVA/PEG hydrogel, the compressive strength as a function of strain was tested. The compressive stress-strain curves of the pure hydrogel and  $\text{MoO}_x$ @MB-hy are presented in Fig. 2e. Compared with pure hydrogel,  $\text{MoO}_x$ @MB-hy slightly increases the compressive stress. Fig. S4b† shows photographs of the hydrogels after the compression and release process, which visually indicates the good mechanical property and elasticity of the hydrogels.

Thermal degradation of  $\text{MoO}_x$ @MB-hy was investigated by a thermogravimetric analysis (TGA) test from 0 to 900 °C. As shown in Fig. 2f, the weight loss process of the hydrogels is

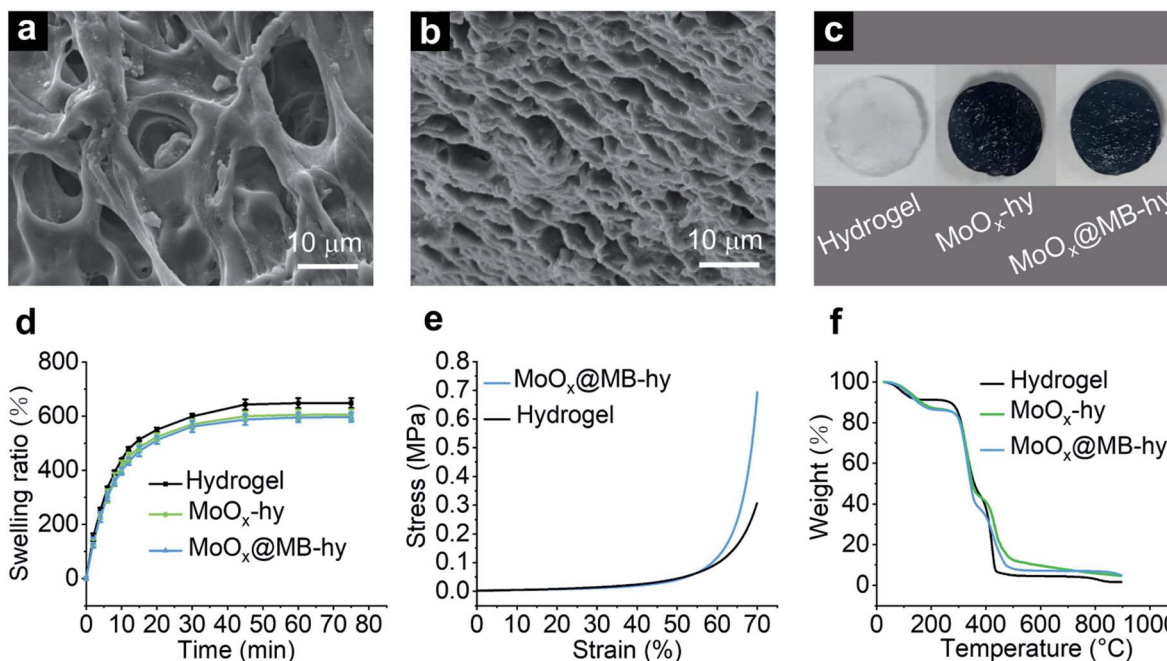


Fig. 2 FE-SEM images of (a) pure hydrogel and (b) MoO<sub>x</sub>@MB-hy. (c) Photographs and (d) swelling behavior of pure hydrogel, MoO<sub>x</sub>-hy and MoO<sub>x</sub>@MB-hy. (e) Compression test of pure hydrogel and MoO<sub>x</sub>@MB-hy. (f) TGA curves of pure hydrogel, MoO<sub>x</sub>-hy and MoO<sub>x</sub>@MB-hy.

divided into two stages. The first mass loss stage is due to the evaporation of absorbed water, indicating the high water-absorption capacity of the hydrogels. The hydrogels show initial decomposition of the chains at  $\sim 250$  °C. The complete decomposition temperature of the hydrogels is at around 450 °C. For the purpose of ensuring safe nanomedicine performance, the degradation performance of MoO<sub>x</sub>@MB-hy was evaluated. Two different pH buffers solutions (pH 7.4 and pH 5.5) were chosen to mimic the physiological and bacterial infection microenvironments, respectively. As shown in Fig. S5a–d,<sup>†</sup> MoO<sub>x</sub> NPs and MoO<sub>x</sub>@MB NPs can be degraded at room temperature in two days at pH 7.4, while they show a relatively slow degradation process over two days at pH 5.5. The degradation behavior of MoO<sub>x</sub> NPs was also demonstrated by TEM. As shown in Fig. S5e,<sup>†</sup> the particle size of MoO<sub>x</sub> NPs at pH 7.4 gradually decreased over two days, while the sizes of NPs at pH 5.5 did not obviously change. Moreover, the evenly distributed MoO<sub>x</sub> NPs in MoO<sub>x</sub>-hy and MoO<sub>x</sub>@MB-hy gradually degraded, and the color of the two hydrogels gradually transformed from dark blue to white and light blue, respectively (Fig. S5f<sup>†</sup>). The hydrogel-loaded MoO<sub>x</sub> NPs were obviously degraded in neutral condition over several days, which suggests that the NPs could be easily metabolized if they were retained on tissues. The good biodegradability of MoO<sub>x</sub> NPs in hydrogels is also beneficial to the disposal of this nanocomposite hydrogel as medical waste.

### 3.4 Photothermal properties

MoO<sub>x</sub> NPs have been demonstrated as good NIR-I and NIR-II photothermal agents for antitumor or antibacterial treatment.<sup>16,19</sup> Thus, we investigated the NIR photothermal

conversion efficiency of MoO<sub>x</sub>@MB NPs. Our results show that MoO<sub>x</sub>@MB NPs present a rapid rise in temperature in response to different concentrations (Fig. 3a and S6a<sup>†</sup>) in the hydrogel and laser irradiation power densities (Fig. 3b) within 10 min. The real-time photothermal images taken by infrared thermal camera also visualize the corresponding temperature change of MoO<sub>x</sub>@MB-hy under 1064 nm laser treatment. Compared with the PBS and hydrogel, MoO<sub>x</sub>@MB-hy exhibits a good photothermal conversion performance (Fig. S6b<sup>†</sup>). Among the various concentrations of MoO<sub>x</sub>@MB NPs in the hydrogels, the temperature of MoO<sub>x</sub>@MB-hy (250  $\mu$ g mL<sup>-1</sup>) can gradually rise to 55 °C upon irradiation with the 1064 nm laser (0.5 W cm<sup>-2</sup>, 10 min). In contrast, MoO<sub>x</sub>@MB-hy under 660 nm laser irradiation (100 mW cm<sup>-2</sup>, 5 min) cannot induce a temperature increase (Fig. S7<sup>†</sup>). Thus, we chose MoO<sub>x</sub>@MB-hy (250  $\mu$ g mL<sup>-1</sup>) for further photostability studies by performing five repeated 10 min-on/off-cycles of 1064 nm laser irradiation. Compared with the temperature variation after the first laser irradiation, the temperature fluctuation of MoO<sub>x</sub>@MB-hy in the following four cycles is negligible (Fig. 3c), illustrating that MoO<sub>x</sub>@MB-hy can be repeatedly used in phototherapy.

### 3.5 NIR-II triggered MB and Mo ion release from MoO<sub>x</sub>@MB-hy

NIR-light-responsive hydrogels can produce heat under NIR irradiation, and then their degree of swelling and the release of encapsulated cargoes are controlled by NIR light, which has wide biomedical applications.<sup>36,52,53</sup> Thus, we visually investigated the remotely triggered decomposition of the hydrogels. The hydrogels were conducted from solution droplets and subsequently used as a plug to hinder the flow of water within



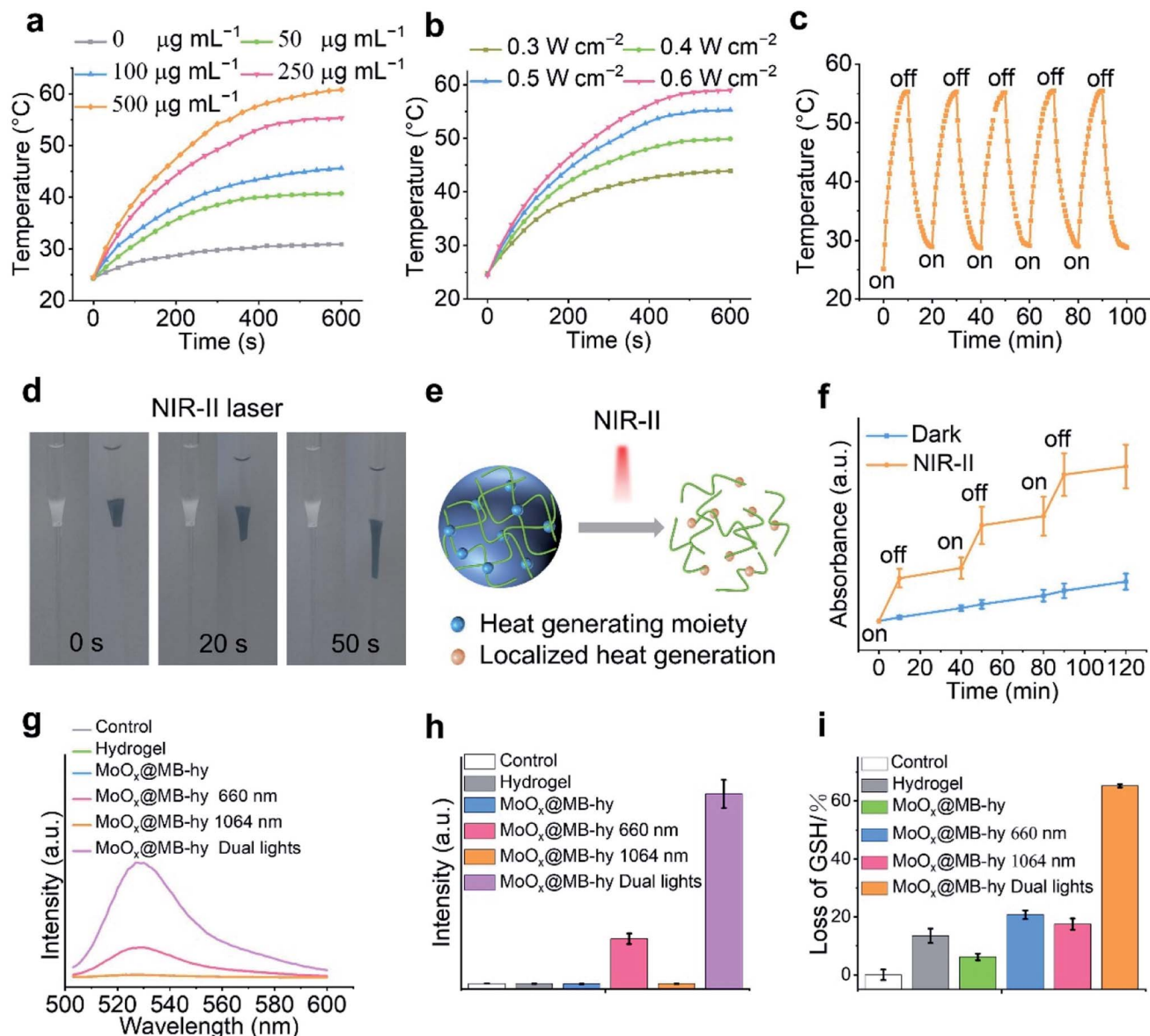


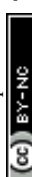
**Fig. 3** (a) Temperature changes of  $\text{MoO}_x@\text{MB-hy}$  with different concentrations under 1064 nm laser irradiation (power density:  $0.5 \text{ W cm}^{-2}$ ). (b) Temperature changes of  $\text{MoO}_x@\text{MB-hy}$  ( $250 \mu\text{g mL}^{-1}$ ) under NIR laser irradiation as a function of power density. (c) Temperature elevation of  $\text{MoO}_x@\text{MB-hy}$  ( $250 \mu\text{g mL}^{-1}$ ) over five NIR-II laser on/off cycles. (d) Proof-of-concept of remotely triggered liquefaction of  $\text{MoO}_x@\text{MB-hy}$  upon NIR-II laser irradiation. (e) Hydrogels containing  $\text{MoO}_x@\text{MB}$  NPs that generate heat in response to an NIR laser are proposed as materials with remotely triggered liquefaction. (f) NIR-II light-triggered MB release from  $\text{MoO}_x@\text{MB-hy}$ . (g and h) Fluorescence spectra and corresponding fluorescence intensities of SOSG after various treatments. (i) Plot of loss of GSH after different irradiation treatments.

a glass Pasteur pipette. As shown in Fig. 3d and S8,† the as-prepared hydrogels without 1064 nm laser irradiation are robust and stable at  $37^\circ\text{C}$  for 2 days. In contrast, upon 1064 nm irradiation,  $\text{MoO}_x@\text{MB-hy}$  undergoes liquefaction within 50 s. This liquefaction is beneficial for exposure of loaded biomaterials in the environment. A schematic diagram of nanomaterial release behavior from the hydrogel composite is shown in Fig. 3e. The controllable release behavior of MB as encapsulated cargo in the hydrogel upon NIR-II laser irradiation is also displayed in Fig. 3f, which could be due to the thermal effect of  $\text{MoO}_x@\text{MB-hy}$  promoting partial diffusion of MB into the solution. Taking advantage of  $\text{MoO}_x$  NPs as an internal heat

source, the triggering of hydrogels by an NIR-II laser could be localized to release MB, offering an opportunity for the intelligent application of local antibacterial PDT. Furthermore, we also found the controlled release of Mo ions from  $\text{MoO}_x@\text{MB-hy}$  under 1064 nm laser irradiation (Fig. S9†).

### 3.6 $^1\text{O}_2$ detection

Reactive oxygen species (ROS), such as  $^1\text{O}_2$ , can effectively damage cell membranes, DNA and cellular proteins. MB has been reported to show high  $^1\text{O}_2$  generation under 650–670 nm laser irradiation, and is often used as a PDT agent.<sup>54</sup> Thus, we employed a fluorescent singlet oxygen sensor green (SOSG)



probe to investigate whether  $\text{MoO}_x@\text{MB}$  can produce toxic  ${}^1\text{O}_2$ . The fluorescence signal of SOSG can react with  ${}^1\text{O}_2$  and then exhibit stronger fluorescence. As expected, in Fig. S10,† the  $\text{MoO}_x@\text{MB}$  NPs hardly produce any  ${}^1\text{O}_2$  under 1064 nm laser irradiation alone. The  ${}^1\text{O}_2$  could be effectively produced by  $\text{MoO}_x@\text{MB}$  NPs under 660 nm laser irradiation or dual-light irradiation. Moreover, the  ${}^1\text{O}_2$  production efficiency of  $\text{MoO}_x@\text{MB}$ -hy with irradiation by different lights was also investigated. Due to the short lifetime and the diffusion length of ROS, it needs to migrate from  $\text{MoO}_x@\text{MB}$  onto the PVA/PEG hydrogel surface to improve its antibacterial efficiency. As shown in Fig. 3g and h, dual-light irradiation could obviously produce much more  ${}^1\text{O}_2$  compared with the  $\text{MoO}_x@\text{MB}$ -hy plus 660 nm group and other groups. Benefiting from the local surface liquefaction (Fig. 3d and e) of  $\text{MoO}_x@\text{MB}$ -hy under 1064 nm laser-induced heat and controlled MB release (Fig. 3f), the  $\text{MoO}_x@\text{MB}$  with homogeneous dispersion rapidly migrates to the hydrogel surface and thus quickly comes close to the bacteria. This process significantly overcomes the intrinsic shortcomings of the short diffusion distance and lifetime of ROS for facilitating the enhanced PDT of  $\text{MoO}_x@\text{MB}$ -hy.

### 3.7 GSH depletion

Oxidative stress in bacteria can be reflected by GSH, which can be converted into oxidized glutathione (GSSG) under oxidative conditions. As can be seen in Fig. 3i, pure hydrogel or  $\text{MoO}_x@\text{MB}$ -hy without any irradiation can cause slight GSH depletion compared with the control. This may be due to a small amount of adsorption of GSH by the hydrogels. GSH treated with  $\text{MoO}_x@\text{MB}$ -hy under 1064 nm or 660 nm laser irradiation can be reduced by about 20%. Due to the various valence states of the Mo-based nanomaterials, especially under NIR-II induced heat and ROS produced under dual-light irradiation, the  $\text{MoO}_x$  NPs from  $\text{MoO}_x@\text{MB}$ -hy could catalyze the oxidation of organic thiol (R-SH) to produce disulfide (R-S-S-R).<sup>55</sup> As expected, the reduction in GSH induced by dual-light irradiation of  $\text{MoO}_x@\text{MB}$ -hy is much higher than that caused by 1064 nm or 660 nm laser irradiation alone. The efficient conversion of GSH to GSSG can destroy the balance of

antioxidants in bacteria and enhance ROS accumulation, which is beneficial for strengthening the antibacterial effect.

### 3.8 Cytotoxicity and hemolytic activity

We used mammalian mouse embryonic fibroblast cell line (NIH3T3) and human umbilical vein endothelial cells (HUVEC) to evaluate the cytotoxicity of  $\text{MoO}_x@\text{MB}$  NPs by a CCK-8 assay. As expected, the  $\text{MoO}_x@\text{MB}$  NPs exhibit relatively low cytotoxicity within 24 h toward NIH3T3 and HUVEC cells. The cell viability is up to over 80% even when treated with 100  $\mu\text{g mL}^{-1}$  of  $\text{MoO}_x@\text{MB}$  NPs (Fig. S11†). The cytotoxicity of  $\text{MoO}_x@\text{MB}$ -hy was also studied using the NIH3T3 and HUVEC cells. The cells were co-cultured with the pure hydrogel and  $\text{MoO}_x@\text{MB}$ -hy extracts. As indicated in Fig. 4a and b, after 24 h of incubation, the cell viabilities of the above two cells are over 85%. Even after 48 h of incubation, the cell viabilities are over 80%. Moreover, hemolytic analysis suggests that all samples treated with hydrogels can produce an ignorable hemolysis (Fig. 4c). Therefore, the hydrogels can be applied as a safe and potential dressing in antibacterial therapy.

### 3.9 *In vitro* antibacterial properties

The antibacterial properties of  $\text{MoO}_x@\text{MB}$ -hy against  $\text{Amp}^r$  *E. coli* and *B. subtilis* under different sources of light irradiation were evaluated by the spread plate counting method. As shown in Fig. 5a–d, most of the bacteria treated with pure hydrogel with or without irradiation are alive. Compared with the control group, the amount of bacteria in pure hydrogel decreases slightly, which can be ascribed to the capture of bacteria by the hydrogel.  $\text{MoO}_x$ -hy under dark conditions or 660 nm irradiation also exhibits no antibacterial activities compared with the control group. However,  $\text{MoO}_x@\text{MB}$ -hy under 660 nm irradiation exhibits antibacterial efficiency of >29.79%. This can be explained by the PDT effect of  $\text{MoO}_x@\text{MB}$ -hy under 660 nm laser irradiation producing a small amount of  ${}^1\text{O}_2$  to partly damage the bacteria. Moreover,  $\text{MoO}_x$ -hy and  $\text{MoO}_x@\text{MB}$ -hy under NIR-II irradiation show strong antibacterial activities (>60.59%) due to the photothermal efficacy. However, compared with the other groups,  $\text{MoO}_x@\text{MB}$ -hy under dual-

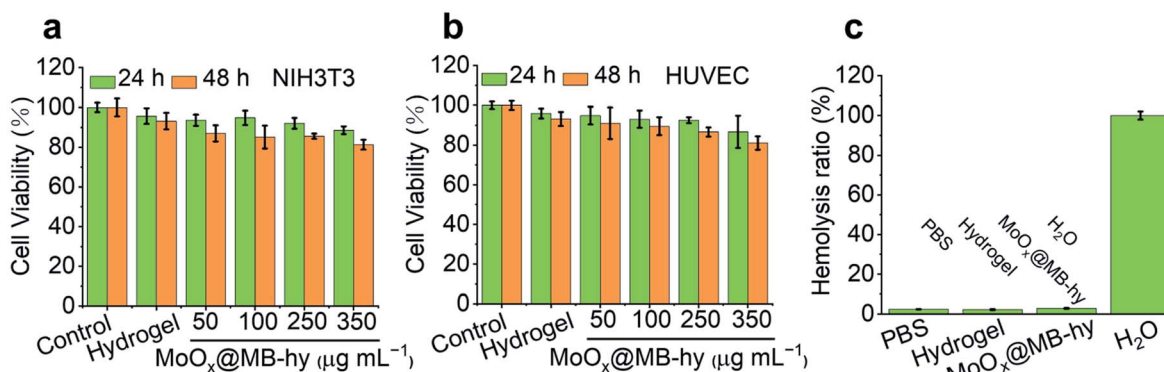


Fig. 4 Cell viabilities of (a) NIH3T3 and (b) HUVEC after co-culture with  $\text{MoO}_x@\text{MB}$ -hy extracts (24 h and 48 h). (c) Relative hemolysis ratio of pure hydrogel,  $\text{MoO}_x@\text{MB}$ -hy ( $250 \mu\text{g mL}^{-1}$ ), PBS and distilled water.



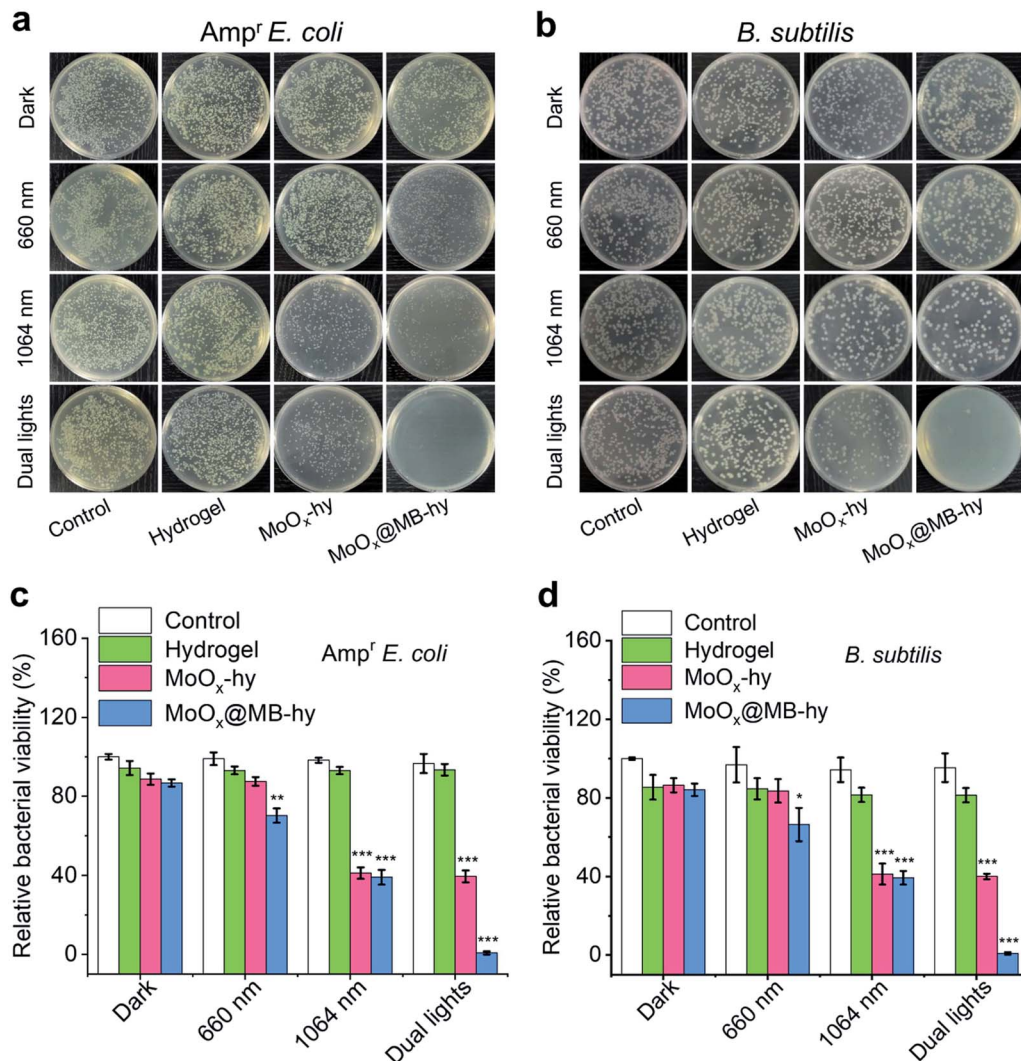


Fig. 5 Photographs of the plated bacterial colonies formed by (a) Amp<sup>r</sup> *E. coli* and (b) *B. subtilis* after different treatments. Relative bacterial viabilities of (c) Amp<sup>r</sup> *E. coli* and (d) *B. subtilis* after different treatments. *p*-values were calculated by the Student's test: \**p* < 0.05, \*\**p* < 0.01, \*\*\**p* < 0.001.

light irradiation exhibits the strongest antibacterial activity against bacteria (99.16%), which implies the good synergistic effect of PTT and PDT.

FE-SEM was employed to observe the morphologies of the Amp<sup>r</sup> *E. coli* and *B. subtilis* given different treatments. As can be seen in Fig. 6a, both Amp<sup>r</sup> *E. coli* and *B. subtilis* are damaged to a certain extent under 1064 nm or 660 nm laser irradiation. However, after dual-light irradiation, the bacteria treated with MoO<sub>x</sub>@MB-hy show severely ruptured cell membranes and even complete loss of integrity, as marked by the red rows. Interestingly, we also evaluated the morphologies of bacteria on the hydrogels. As shown in Fig. S12,† some bacteria adhering to the surface of hydrogels can be observed, which is consistent with the above data. The bacteria on pure hydrogel are not obviously damaged, while the bacteria on MoO<sub>x</sub>@MB-hy are impaired. Furthermore, to analyze the membrane integrity of the bacteria after different treatments, SYTO-9/PI dual fluorescence staining was utilized. The bacterial cells in the control, hydrogel and

MoO<sub>x</sub>@MB-hy groups without any irradiation exhibit green fluorescence, suggesting that the bacteria still have complete cell membranes (Fig. 6b). However, the bacteria in the MoO<sub>x</sub>@MB-hy groups treated with 1064 nm/660 nm laser irradiation show some red fluorescence, suggesting partial damage to the bacteria. The strongest red fluorescence of bacteria can be observed in the group of MoO<sub>x</sub>@MB-hy plus dual-light irradiation, indicating the severe destruction of the bacterial membranes. These results further prove that the damage to bacterial membranes achieved by the synergistic effect of PTT and PDT of MoO<sub>x</sub>@MB-hy dressing can account for the excellent antibacterial ability.

### 3.10 Wound healing and biosafety evaluation

We next employed an Amp<sup>r</sup> *E. coli* infected mouse model to assess the therapeutic potential of MoO<sub>x</sub>@MB-hy. The experiments were divided into six groups: PBS, kanamycin (Kana), pure hydrogel, MoO<sub>x</sub>@MB-hy (660 nm), MoO<sub>x</sub>@MB-hy (1064 nm) and



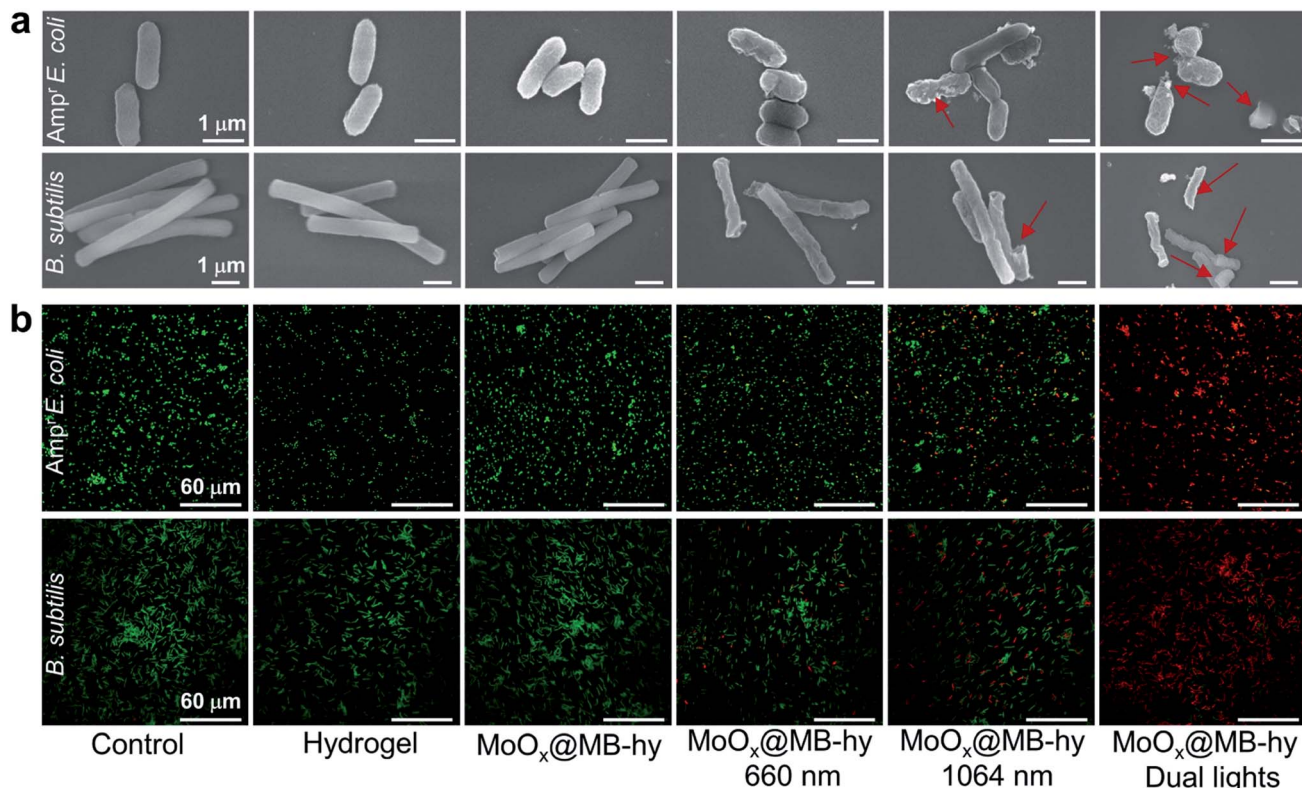


Fig. 6 (a) Morphologies observation of *Amp<sup>r</sup> E. coli* and *B. subtilis* after different treatments by FE-SEM. (b) PI and SYTO 9 double staining of *Amp<sup>r</sup> E. coli* and *B. subtilis* after various treatments.

MoO<sub>x</sub>@MB-hy (dual lights). It is worth mentioning that Kana is a common antibiotic used to treat diverse infections, especially in anti-infection treatment of the skin.<sup>45</sup> The treatment process and timeline of the hydrogel-based antibacterial therapy are shown in Fig. 7a. After exposure to 1064 nm irradiation, the representative thermographic images of temperature change in MoO<sub>x</sub>@MB-hy were captured by an FLIR photothermal camera. The temperature of MoO<sub>x</sub>@MB-hy in the wound site increased sharply, from 34 to 43 °C (Fig. 7b), which is a mild temperature for killing the bacteria around the wound.<sup>56,57</sup> After antibacterial treatments, the evolution of the infected wound was recorded for 10 days. The wounds were photographed on days 0, 6 and 10 (Fig. 7c). The wound closures in all groups show that the MoO<sub>x</sub>@MB-hy (dual lights) group can promote wound healing faster than the other groups after 6 days and after 10 days (Fig. 7d). As for the antibacterial effect *in vivo*, the number of bacteria in the wounds treated with MoO<sub>x</sub>@MB-hy (660 nm) or MoO<sub>x</sub>@MB-hy (1064 nm) can be reduced to a certain extent, but there are still many live bacteria. However, quantity of bacteria in the wounds treated with MoO<sub>x</sub>@MB-hy plus dual-lights decreases significantly (Fig. 7e and f).

The regenerated epidermis at the wounds was assessed by histological analysis. Inflammatory reaction and wound repair were evaluated by hematoxylin and eosin (H&E) staining. An inflammatory response and connective tissue loss were observed in all groups on day 2 of H&E staining. As shown in Fig. 8, on day 10, there are lots of inflammatory cells and

incomplete re-epithelialization in soft tissues of the PBS, Kana and pure hydrogel treated groups. In the groups of MoO<sub>x</sub>@MB-hy (1064 nm) and MoO<sub>x</sub>@MB-hy (660 nm), the number of inflammatory cells decreases significantly, but the connective tissue and epithelial layer are defective to some extent. However, the wounds from the MoO<sub>x</sub>@MB-hy (dual lights) group show the fewest inflammatory cells and a well-organized stratified epithelial layer. Moreover, collagen formation and deposition were evaluated by Masson staining. As shown in Fig. S13,† on day 2, the collagen deposition in each group is sparsely distributed. On day 10, the wounds in groups of control, Kana, pure hydrogel, MoO<sub>x</sub>@MB-hy (1064 nm), and MoO<sub>x</sub>@MB-hy (660 nm) exhibit small blue-dyed areas and poorly-developed shattered collagen bundles. However, in the MoO<sub>x</sub>@MB-hy (dual lights) group, the collagen bundles are better, and blue staining is visible in full-thickness dermal wounds.

In the process of antibacterial treatment, we also conducted a preliminary biosafety assessment. Body weight changes were similar between treatment groups and healthy mice (Fig. S14†). Furthermore, after the treatment, serum biochemical analysis and routine blood of the mice were studied to evaluate the biosafety of MoO<sub>x</sub>@MB-hy (dual lights) in mice. Compared with the non-wounded healthy group, the blood parameters of mice in the MoO<sub>x</sub>@MB-hy (dual lights) group were all within the normal range, indicating the high biocompatibility of MoO<sub>x</sub>@MB-hy (dual lights) (Fig. S15†). Finally, the major organs



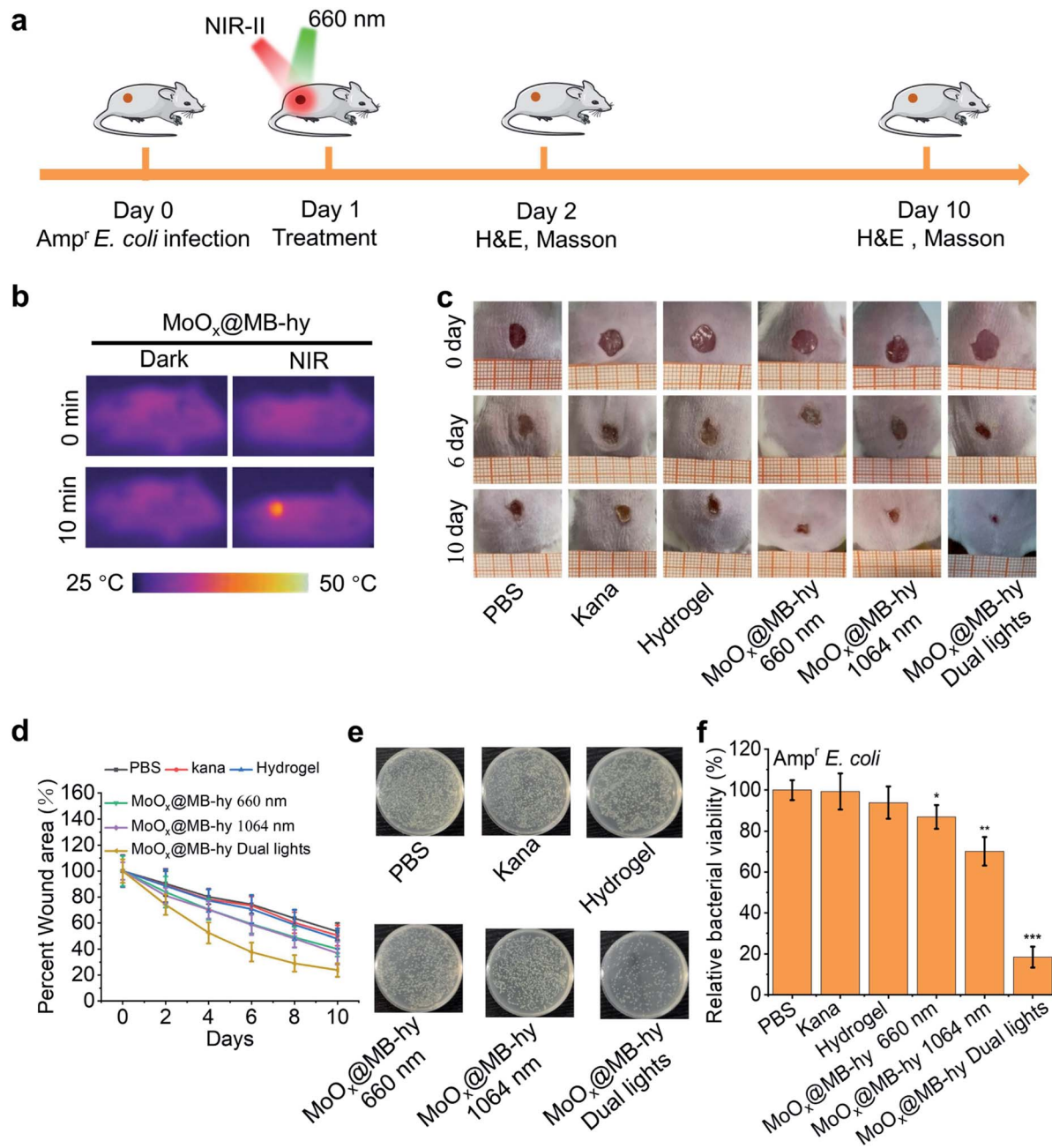


**Fig. 7** (a) Schematic illustration for the construction of  $\text{Amp}' E. coli$ -infected wound model and treatment procedure of mice. (b) Infrared thermal images of  $\text{Amp}' E. coli$ -infected mice after treatment with  $\text{MoO}_x@\text{MB-hy}$  under NIR-II (1064 nm) laser irradiation ( $0.3 \text{ W cm}^{-2}$ ). (c) Photographs of  $\text{Amp}' E. coli$ -infected areas after different treatments and (d) wound area of mice. (e) Photographs of plated bacterial colonies obtained from infected skin tissues of mice at day 2 and (f) corresponding statistical analysis of the bacterial viability.  $p$ -values were calculated by the Student's test: \* $p$  < 0.05, \*\* $p$  < 0.01, \*\*\* $p$  < 0.001.

(heart, liver, spleen, lung, and kidney) taken from the  $\text{MoO}_x@\text{MB-hy}$  (dual lights) treated mice on the tenth day were investigated using H&E staining. The structures of these organs were normal with no obvious difference from those of healthy group (Fig. S16†).

The  $\text{MoO}_x@\text{MB-hy}$  as a safe and multifunctional dressing can avoid the aggregation of  $\text{MoO}_x@\text{MB}$  NPs alone. Meanwhile, 1064 nm laser-induced heat enhances the controllable MB release from the surface liquefaction of  $\text{MoO}_x@\text{MB-hy}$  to

produce the most  ${}^1\text{O}_2$  under 660 nm irradiation quickly. Importantly, negatively charged  $\text{MoO}_x@\text{MB}$  and a bacteria-infected acidic wound microenvironment have a strong interaction. During the rapid surface-liquefaction synergistic PTT-PDT, porous  $\text{MoO}_x@\text{MB-hy}$  can not only absorb some of the bacteria but can also trap the bacteria to the limit of ROS damage and deplete GSH to achieve self-migration-enhanced ROS accumulation on bacteria from the wound. Consequently, the intrinsic shortcomings of short diffusion distance



## H&amp;E

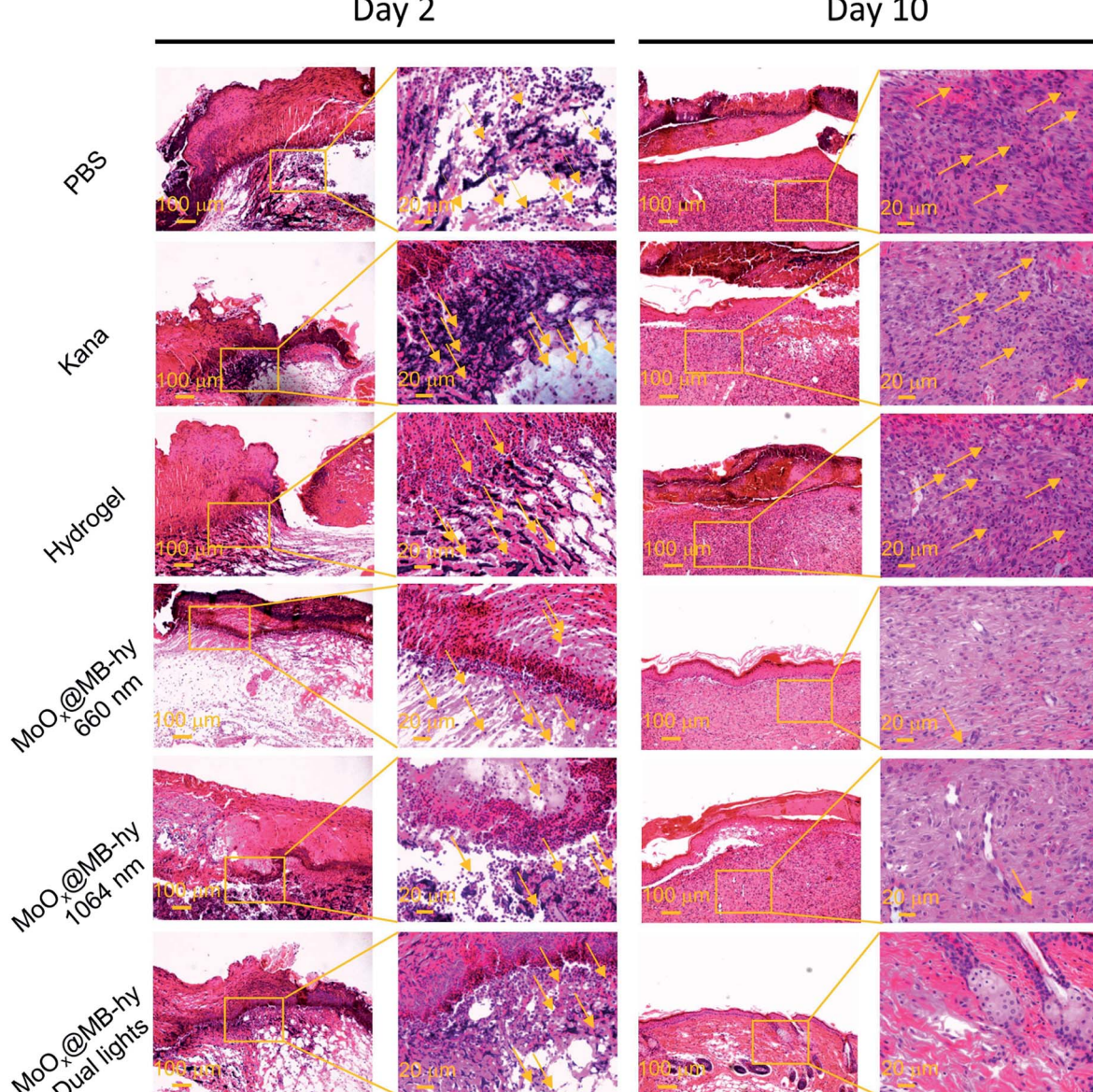


Fig. 8 H&E staining images of infected wound tissues after various treatments.

and lifetime of ROS are conquered. In particular, the dual-light-activatable antibacterial process largely promotes the healing of wounds infected by drug-resistant bacteria.

#### 4. Conclusions

In summary, we developed a novel, biocompatible phototheranostic nanocomposite hydrogel ( $\text{MoO}_x@\text{MB-hy}$ ) dressing with synergistic PTT-PDT to treat wounds infected by drug-resistant bacteria. Due to the strong NIR-II light absorption, the  $\text{MoO}_x@\text{MB-hy}$ -induced heat achieved rapid surface liquefaction and controlled the release of MB. Then, under 660 nm laser irradiation,  $\text{MoO}_x@\text{MB-hy}$  can effectively produce more

$^1\text{O}_2$ .  $\text{MoO}_x@\text{MB-hy}$  can simultaneously deplete GSH antioxidant and trap the bacteria to the distance limit of ROS damage, conquering the intrinsic shortcomings of short diffusion distance and lifetime of ROS to improve ROS accumulation, leading to strengthened bacterial membrane permeability and sterilizing effect. An *in vitro* antibacterial study showed that  $\text{MoO}_x@\text{MB-hy}$  under dual-light irradiation can effectively eliminate Gram Amp<sup>r</sup> *E. coli* and *B. subtilis* in only 15 min. Animal experiments demonstrated that  $\text{MoO}_x@\text{MB-hy}$  can accelerate healing of wounds infected by Amp<sup>r</sup> *E. coli*. Therefore, this study provides a novel phototheranostic strategy based on dual-light-activatable hydrogel dressing with great potential for treating drug-resistant bacterial infections.

## Conflicts of interest

There are no conflicts to declare.

## Acknowledgements

This work was supported by the National Natural Science Foundation of China (U1932112, 22175182), the Sheng Yuan Cooperation (2021SYHZ0048), the Beijing Natural Science Foundation (2202064), the Natural Science Foundation of Ningxia (2020AAC03115), the CAS Light of West China Program (XAB2020YW16) and the Scientific Research Project of the Ningxia Higher Education Institutions of China (NGY2020034).

## References

- 1 K. E. Jones, N. G. Patel, M. A. Levy, A. Storeygard, D. Balk, J. L. Gittleman and P. Daszak, *Nature*, 2008, **451**, 990–993.
- 2 B. D. Lushniak, *Public Health Rep.*, 2014, **129**, 314–316.
- 3 M. J. Culyba and D. Van Tyne, *PLoS Pathog.*, 2021, **17**, 1009872.
- 4 J. Xie, L. Gong, S. Zhu, Y. Yong, Z. Gu and Y. Zhao, *Adv. Mater.*, 2019, **31**, 1802244.
- 5 L. Yan, F. Zhao, J. Wang, Y. Zu, Z. Gu and Y. Zhao, *Adv. Mater.*, 2019, **31**, 1805391.
- 6 L. Mei, S. Zhu, Y. Liu, W. Yin, Z. Gu and Y. Zhao, *Chem. Eng. J.*, 2021, **418**, 129431.
- 7 Y. Zu, H. Yao, Y. Wang, L. Yan, Z. Gu, C. Chen, L. Gao and W. Yin, *VIEW*, 2021, **2**, 20200188.
- 8 T. Wang, X. Zhang, L. Mei, D. Ma, Y. Liao, Y. Zu, P. Xu, W. Yin and Z. Gu, *Nanoscale*, 2020, **12**, 8415–8424.
- 9 G. Gorle, A. Bathinapatla, Y. Z. Chen and Y. C. Ling, *RSC Adv.*, 2018, **8**, 19827–19834.
- 10 W. Yin, J. Yu, F. Lv, L. Yan, L. R. Zheng, Z. Gu and Y. Zhao, *ACS Nano*, 2016, **10**, 11000–11011.
- 11 X. Zhang, H. Li, Q. Li, Y. Li, C. Li, M. Zhu, B. Zhao and G. Li, *World J. Surg. Oncol.*, 2018, **16**, 222.
- 12 Y. Xiang, C. Mao, X. Liu, Z. Cui, D. Jing, X. Yang, Y. Liang, Z. Li, S. Zhu, Y. Zheng, K. W. K. Yeung, D. Zheng, X. Wang and S. Wu, *Small*, 2019, **15**, e1900322.
- 13 X. Zhang, G. Zhang, H. Zhang, X. Liu, J. Shi, H. Shi, X. Yao, P. K. Chu and X. Zhang, *Chem. Eng. J.*, 2020, **382**, 122849.
- 14 Q. Cui, H. Yuan, X. Bao, G. Ma, M. Wu and C. Xing, *ACS Appl. Bio Mater.*, 2020, **3**, 4436–4443.
- 15 G. Duan, L. Wen, X. Sun, Z. Wei, R. Duan, J. Zeng, J. Cui, C. Liu, Z. Yu, X. Xie and M. Gao, *Small*, 2021, 2107137.
- 16 Y. Zhang, D. Li, J. Tan, Z. Chang, X. Liu, W. Ma and Y. Xu, *Small*, 2020, **17**, e2005739.
- 17 B. Yu, W. Wang, W. Sun, C. Jiang and L. Lu, *J. Am. Chem. Soc.*, 2021, **143**, 8855–8865.
- 18 R. Hille, J. Hall and P. Basu, *Chem. Rev.*, 2014, **114**, 3963–4038.
- 19 W. Yin, T. Bao, X. Zhang, Q. Gao, J. Yu, X. Dong, L. Yan, Z. Gu and Y. Zhao, *Nanoscale*, 2018, **10**, 1517–1531.
- 20 Z. Zhou, Y. Wang, F. Peng, F. Meng, J. Zha, L. Ma, Y. Du, N. Peng, L. Ma, Q. Zhang, L. Gu, W. Yin, Z. Gu and C. Tan, *Angew. Chem., Int. Ed.*, 2022, e202115939.
- 21 Y. S. Dong, S. M. Dong, Z. Wang, L. L. Feng, Q. Q. Sun, G. Y. Chen, F. He, S. K. Liu, W. T. Li and P. P. Yang, *ACS Appl. Mater. Interfaces*, 2020, **12**, 52479–52491.
- 22 Z. Yu, W. K. Chan, Y. Zhang and T. T. Y. Tan, *Biomaterials*, 2021, **269**, 120459.
- 23 M. R. Hamblin, *Curr. Opin. Microbiol.*, 2016, **33**, 67–73.
- 24 Y. Zhou, W. M. Deng, M. L. Mo, D. X. Luo, H. H. Liu, Y. Jiang, W. J. Chen and C. S. Xu, *Front. Med.*, 2021, **8**, 8.
- 25 E. Klepsyte and N. E. Samalavicius, *Tech. Coloproctol.*, 2012, **16**, 207–211.
- 26 P. Rodriguez, A. P. Singh, K. E. Malloy, W. Zhou, D. W. Barrett, C. G. Franklin, W. B. Altmeyer, J. E. Gutierrez, J. Li, B. L. Heyl, J. L. Lancaster, F. Gonzalez-Lima and T. Q. Duong, *Brain Imaging Behav.*, 2017, **11**, 640–648.
- 27 S. Khan, S. N. Khan, R. Meena, A. M. Dar, R. Pal and A. U. Khan, *J. Photochem. Photobiol. B*, 2017, **174**, 150–161.
- 28 S. Khan, F. Alam, A. Azam and A. U. Khan, *Int. J. Nanomed.*, 2012, **7**, 3245–3257.
- 29 P. Parasuraman, R. Y. Thamanna, C. Shaji, A. Sharan, A. H. Bahkali, H. F. Al-Harthi, A. Syed, V. T. Anju, M. Dyavaiah and B. Siddhardha, *Pharmaceutics*, 2020, **12**, 709.
- 30 W. A. Pryor, *Annu. Rev. Physiol.*, 1986, **48**, 657–667.
- 31 S. Hatz, J. D. C. Lambert and P. R. Ogilby, *Photochem. Photobiol. Sci.*, 2007, **6**, 1106–1116.
- 32 X. Zhang, L. Y. Xia, X. Chen, Z. Chen and F. G. Wu, *Sci. China Mater.*, 2017, **60**, 487–503.
- 33 G. Gao, Y. W. Jiang, H. R. Jia and F. G. Wu, *Biomaterials*, 2019, **188**, 83–95.
- 34 Y. Chen, Y. Qiu, Q. Wang, D. Li, T. Hussain, H. Ke and Q. Wei, *Chem. Eng. J.*, 2020, **399**, 125668.
- 35 Y. Liu, Y. Xiao, Y. Cao, Z. Guo, F. Li and L. Wang, *Adv. Funct. Mater.*, 2020, **30**, 2003196.
- 36 M. Mu, X. L. Li, A. P. Tong and G. Guo, *Expert Opin. Drug Delivery*, 2019, **16**, 239–250.
- 37 A. Karimi and M. Navidbakhsh, *Mater. Technol.*, 2014, **29**, 90–100.
- 38 J. S. Suk, Q. Xu, N. Kim, J. Hanes and L. M. Ensign, *Adv. Drug Delivery Rev.*, 2016, **99**, 28–51.
- 39 Z. Zhang, Z. Ye, F. Hu, W. Wang, S. Zhang, L. Gao and H. Lu, *J. Appl. Polym. Sci.*, 2022, **139**, e51563.
- 40 S. Ahmed, U. K. Mandal, M. Taher, D. Susanti and J. M. Jaffri, *Pharm. Dev. Technol.*, 2018, **23**, 751–760.
- 41 X. Xiao, G. Wu, H. Zhou, K. Qian and J. Hu, *Polymers*, 2017, **9**, 259.
- 42 P. Parasuraman, V. T. Anju, S. B. Sruthil Lal, A. Sharan, S. Busi, K. Kaviyarasu, M. Arshad, T. M. S. Dawoud and A. Syed, *Photochem. Photobiol. Sci.*, 2019, **18**, 563–576.
- 43 S. L. Pedersen, T. H. Huynh, P. Pöschko, A. S. Fruergaard, M. T. Jarlstad Olesen, Y. Chen, H. Birkedal, G. Subbiahdoss, E. Reimhult, J. Thøgersen and A. N. Zelikin, *ACS Nano*, 2020, **14**, 9145–9155.
- 44 W. Liu, W. Ou-Yang, C. Zhang, Q. Wang, X. Pan, P. Huang, C. Zhang, Y. Li, D. Kong and W. Wang, *ACS Nano*, 2020, **14**, 12905–12917.



45 Z. Guo, J. X. He, S. H. Mahadevegowda, S. H. Kho, M. B. Chan-Park and X. W. Liu, *Adv. Healthcare Mater.*, 2020, **9**, 2000265.

46 Z. Xu, K. Yao, H. Fu, X. Shen, X. Duan, L. Cao, J. Huang and H. Wang, *Global Challenges*, 2017, **1**, 1700050.

47 J. Xu, M. Mao and H. Yu, *Res. Chem. Intermed.*, 2020, **46**, 1823–1840.

48 A. Mekki, G. D. Khattak and L. E. Wenger, *J. Non-Cryst. Solids*, 2005, **351**, 2493–2500.

49 X. Li, Y. Wang, J. Wang, Y. Da, J. Zhang, L. Li, C. Zhong, Y. Deng, X. Han and W. Hu, *Adv. Mater.*, 2020, **32**, 2003414.

50 Y. Li, J. Wang, Y. Yang, J. Shi, H. Zhang, X. Yao, W. Chen and X. Zhang, *Mater. Sci. Eng., C*, 2021, **118**, 111447.

51 A. Khalilipour and A. Paydayesh, *J. Macromol. Sci., Part B: Phys.*, 2019, **58**, 371–384.

52 L. Kuang, J. Huang, Y. Liu, X. Li, Y. Yuan and C. Liu, *Adv. Funct. Mater.*, 2021, **31**, 2105383.

53 Y. P. Jia, K. Shi, F. Yang, J. F. Liao, R. X. Han, L. P. Yuan, Y. Hao, M. Pan, Y. Xiao, Z. Y. Qian and X. W. Wei, *Adv. Funct. Mater.*, 2020, **30**, 2001059.

54 M. Wainwright, *Photodiagn. Photodyn. Ther.*, 2005, **2**, 263–272.

55 S. Terpilowska and A. K. Siwicki, *Chem.-Biol. Interact.*, 2019, **298**, 43–51.

56 W. Niu, M. Chen, Y. Guo, M. Wang, M. Luo, W. Cheng, Y. Wang and B. Lei, *ACS Nano*, 2021, **15**, 14323–14337.

57 X. Lin, Y. Fang, Z. Hao, H. Wu, M. Zhao, S. Wang and Y. Liu, *Small*, 2021, 2103303.

